PAPER

The scalar, vector, and tensor modes in gravitational wave turbulence simulations

View the article online for updates and enhancements.

The scalar, vector, and tensor modes in gravitational wave turbulence simulations

Axel Brandenburg[1,2,3,4] , **Grigol Gogoberidze**[4] ,
Tina Kahniashvili[3,4,5,6] , **Sayan Mandal**[4,7,*] ,
Alberto Roper Pol[4,8] **and Nakul Shenoy**[9]

[1] Nordita, KTH Royal Institute of Technology and Stockholm University, Hannes Alfvéns vägen 12, 10691 Stockholm, Sweden
[2] Department of Astronomy, AlbaNova University Center, Stockholm University, 10691 Stockholm, Sweden
[3] Department of Physics and McWilliams Center for Cosmology, Carnegie Mellon University, 5000 Forbes Ave, Pittsburgh, PA 15213, United States of America
[4] School of Natural Sciences and Medicine, Ilia State University, 3-5 Cholokashvili Street, 0194 Tbilisi, Georgia
[5] Department of Physics, Laurentian University, Sudbury, ON P3E 2C, Canada
[6] Abastumani Astrophysical Observatory, 47/57 Kostava Street, Tbilisi GE-0179, Georgia
[7] Physics and Astronomy Department, Stony Brook University, 100 Nicolls Road, Stony Brook, New York 11794, United States of America
[8] Université de Paris, CNRS, Astrophysique et Cosmologie, Paris, F-75013, France
[9] Department of Physics, Massachusetts Institute of Technology, Cambridge, MA 02139, United States of America

E-mail: brandenb@nordita.org, grigol_gogoberidze@iliauni.edu.ge, tinatin@andrew.cmu.edu, sayan.mandal@stonybrook.edu, roperpol@apc.in2p3.fr and getnakul@mit.edu

CrossMark

Abstract

We study the gravitational wave (GW) signal sourced by primordial turbulence that is assumed to be present at cosmological phase transitions like the electroweak and quantum chromodynamics phase transitions. We consider various models of primordial turbulence, such as those with and without helicity, purely hydrodynamical turbulence induced by fluid motions, and magnetohydrodynamic turbulence whose energy can be dominated either by kinetic or magnetic energy, depending on the nature of the turbulence. We also study circularly polarized GWs generated by parity violating sources such as helical turbulence. Our ultimate goal is to determine the efficiency of GW production through different classes of turbulence. We find that the GW energy and strain tend to be

*Author to whom any correspondence should be addressed.

large for acoustic or irrotational turbulence, even though its tensor mode amplitude is relatively small at most wave numbers. Only at very small wave numbers is the spectral tensor mode significant, which might explain the efficient GW production in that case.

(Some figures may appear in colour only in the online journal)

1. Introduction

Gravitational waves (GWs) can provide a window into the earliest epochs of the Universe when it was opaque to electromagnetic radiation (see reference [1], chapters: 21–22). Being massless and decoupled from other physical interactions (weak, strong, and electromagnetic), GWs propagate *almost*[9] freely after their generation preserving their spectral characteristics and diluting only with the expansion of the Universe. In particular, cosmological GW backgrounds produced by magnetohydrodynamic (MHD) turbulence conserve the characteristics of the source, i.e., the spectral peak and the energy density of the produced GW signal can be related to the characteristic scale and total energy density of the sourcing magnetic or velocity field at the time of generation (with a precision of about one order of magnitude for the energy density depending on the duration of the turbulence sourcing) [10].

If GWs are generated during the early Universe at energy scales around the electroweak (EW) and quantum chromodynamics (QCD) phase transitions are detected, they will carry information about the fundamental physical processes at play when the Universe was only 10^{-11} and 10^{-5} s old, respectively. The laser interferometer space antenna, slated to launch in 2034, will be sensitive to GWs generated around the 100 GeV–1 TeV scale (see references [11–13] for pioneering works and reference [14] for a recent review and reference therein). It is also conceivable that the GWs generated at the EW epoch can be detected in atomic interferometry experiments [15], and those originated at the QCD epoch (or around) at typical frequencies of 10^{-7}–10^{-9} Hz in pulsar timing array (PTA) experiments [16–18]. Indeed PTAs provide detection of GW signals in the nHz regime making the GW signal arising at the QCD energy scale accessible. Recently, the NANOGrav collaboration has reported strong evidence detection of a signal which could be compatible with a stochastic GW background [19]. If this detection is confirmed in the future, it could be a manifestation of the stochastic GW background originated from the epoch around the QCD energy scale [20–29]. Interestingly, these GWs might be sourced by and reveal the presence of primordial magnetic fields (PMFs) and turbulent motions at the QCD scale [21, 27][10].

Stochastic relic GW backgrounds can be generated through different violent processes in the early Universe, such as amplification of quantum-mechanical fluctuations during inflation, topological defects, cosmic strings, and cosmological phase transitions; see reference [32] for a review and references therein. In the case of cosmological phase transitions, GWs are generated either from the collision of bubbles during first order phase transitions, like the EW or QCD phase transitions (see references [12, 13] for pioneering works), or from the hydrodynamic and MHD turbulence produced in association with the generation of PMFs and turbulence at

---

[9] We discard the damping due to neutrino free streaming [2–8] or from anisotropic stresses [9].

[10] The commonly discussed sources of GWs in the nHz regime are mergers of supermassive black holes [19, 30, 31].

those early times; see references [9, 33, 34] for pioneering works, and for a recent review, see section 8 of reference [32] and references therein.

In this paper we focus on possible turbulent sources in the early Universe, and the applicability of the formalism developed here is independent of the nature of the origin of the turbulence. Additionally, our approach might be used when studying superfluid turbulence in neutron stars, and the GWs emitted by this process must be accounted for when estimating the continuous GW spectrum; see reference [35] for pioneering work and section 6 of reference [36] for a review and references therein.

The consideration of PMFs (and correspondingly turbulent motions) is motivated by observations of blazar spectra by the Fermi gamma-ray observatory. They indicate the presence of magnetic fields at extragalactic scales (see reference [37] for a pioneering work and references [38, 39] for recent studies)[11]. The high conductivity of the early Universe plasma ensures strong coupling between magnetic fields and fluid motions, so the presence of primordial magnetic seeds inevitably results in the development of turbulence [43, 44]. This turbulence can also reinforce the magnetic field; see reference [45] for a discussion of the dynamo mechanism in decaying turbulence. *Any other* turbulent processes in the early Universe can also amplify the magnetic field through dynamo action. The stochastic magnetic fields and the turbulent velocity fields of the primordial plasma contribute to the anisotropic stress tensor that sources the primordial GWs. In addition there might be parity violating (or CP violating) processes in the early Universe that lead to the generation of helical magnetic fields or helical turbulent motions, and thus produce circularly polarized GWs [46]. In particular, the detection of circularly polarized GWs will shed light on phenomena of fundamental symmetry breaking in the early Universe, such as parity violation, and potentially can serve as an explanation of the lepto- and baryogenesis problems (see references [47–50] for pioneering works, and reference [51] for a recent review).

In the present work, we study the scalar, vector, and tensor mode decomposition of different turbulence sources with the objective to help understand their efficiency in producing GWs. More precisely we have considered different classes of turbulence that may be realized in the early Universe. In particular we have studied kinetically and magnetically dominant helical and non-helical cases as well as two types of acoustic turbulence. The latter type consists of interacting sound waves. At large enough Mach numbers, the flow is dominated by shocks. Notably it was shown that the efficiency of sound waves as a source generating relic GWs is not only comparable but exceeds that from bubble collisions; see reference [52] for a pioneering work, and reference [53] for a recent study and references therein. However the generation mechanism related to sound waves requires a first order PT. The ultimate goal of the work presented here is to determine the physical conditions in the early Universe that reach maximal efficiency of the GW signal production *without* being limited by the first order PT consideration. We also study helical versus non-helical sources behavior, and we confirm that, for distinguishing between parity conserving and parity violating sources, the measurement of polarization degrees in the low frequency tail of the spectrum could be used to identify the inverse cascade (which applies to the helical turbulence case) versus the slow inverse transfer.

This paper is arranged as follows. In section 2, we briefly review the decomposition of the MHD stress tensor sourcing the GWs into the scalar, vector, and tensor components, and provide a background on the modeling of turbulent sources. This is followed by detailed numerical modeling for several types of turbulent hydrodynamic and/or MHD flows in section 3. In

---

[11] Also see reference [40] for discussions on possible uncertainties in the measurements of blazar spectra and references [41, 42] on possible impacts of plasma instabilities.

section 4, we describe in brief the degree of circular polarization of both the source and the generated GWs, and present numerical simulations of the degree of polarization of the source. Finally in section 5, we present our conclusions. Throughout this work, we set $\hbar = c = k_{\mathrm{B}} = 1$, and use the metric signature $(-, +, +, +)$. We also set the permeability of free space to unity, i.e., $\mu_0 = 1$, expressing the electromagnetic quantities in Lorentz–Heaviside units. Repeated indices denote a summation, unless otherwise specified. Greek indices run over spacetime coordinates, while Latin indices run over spatial coordinates.

2. Formalism

The stress tensor that sources GWs in the early Universe receives contributions from PMFs [9], as well as the turbulent velocity field of the primordial plasma [54, 55], and the dynamics of phase transitions [11–13]. In the following subsection, we discuss the decomposition of the stress tensor into its scalar, vector, and tensor (i.e., the transverse–traceless (TT)) components[12], following the prescription by Lifshitz [57], and in the next subsection, we will present a brief overview of the different types of turbulent sources. Readers who are familiar with the mechanism of scalar–vector–tensor (SVT) decomposition can skip ahead to section 2.4.

2.1. The SVT decomposition of the stress tensor

According to the Lifshitz prescription, any symmetric rank-2 tensor $\lambda_{ij}(\mathbf{x})$ in d-dimensions can be decomposed as [59]

$$\lambda_{ij} = L\delta_{ij} + \nabla_{\langle i}\nabla_{j\rangle}\lambda + \nabla_{(i}\bar{\lambda}_{j)} + \bar{\lambda}_{ij}, \tag{1}$$

where $\bar{\lambda}_i$ is divergenceless, $\nabla_i\bar{\lambda}_i = 0$, $\bar{\lambda}_{ij}$ is divergenceless and traceless,

$$\nabla_i\bar{\lambda}_{ij} = \nabla_j\bar{\lambda}_{ij} = 0, \quad \bar{\lambda}_{ii} = 0, \tag{2}$$

and

$$\nabla_{\langle i}\nabla_{j\rangle}\lambda \equiv \left(\nabla_i\nabla_j - \frac{1}{d}\delta_{ij}\nabla^2\right)\lambda, \tag{3}$$

$$\nabla_{(i}\bar{\lambda}_{j)} \equiv \frac{1}{2}\left(\nabla_i\bar{\lambda}_j + \nabla_j\bar{\lambda}_i\right), \tag{4}$$

correspond to the removal of trace, and the symmetrization operators, respectively. This decomposition is commonly referred to as a SVT decomposition. Extracting the components in real space is algebraically involved, and is discussed in detail in appendix A.

The process, however, is less cumbersome in momentum space where the analog of equation (1) can be written as,

$$\tilde{\lambda}_{ij} = \tilde{L}\delta_{ij} - k_{\langle i}k_{j\rangle}\tilde{\lambda}^S + ik_{(i}\tilde{\lambda}^V_{j)} + \tilde{\lambda}^T_{ij}, \tag{5}$$

where tildes denote quantities in Fourier space[13], k_i is the ith component of $\mathbf{k}$, and the superscripts S, V, and T denote the scalar, vector, and tensor contributions respectively. Analogous to the real space expressions, we have $k_i\tilde{\lambda}^V_i = 0$, $k_i\tilde{\lambda}^T_{ij} = k_j\tilde{\lambda}^T_{ij} = 0$, and $\tilde{\lambda}^T_{ii} = 0$, $k_{\langle i}k_{j\rangle} \equiv$

---

[12] This is not to be conflated with the TT gauge in which the GWs are computed far from the source.

[13] We also adopt the notational convention that a function $f(\mathbf{r})$ of real space coordinates $\mathbf{r}$ is expressed in terms of its Fourier transform $\tilde{f}(\mathbf{k})$ as $f(\mathbf{r}) = (2\pi)^{-3}\int \mathrm{d}^3\mathbf{k}\, \mathrm{e}^{-i\mathbf{k}\cdot\mathbf{r}}\tilde{f}(\mathbf{k})$, and the inverse transform is defined accordingly.

$k_i k_j - k^2 \delta_{ij}/d$ with $k = |\mathbf{k}|$, and the parentheses in the indices denote a symmetrization as in equation (3). $\tilde{L}$ is proportional to the trace, i.e., $\tilde{L} = \tilde{\lambda}_{ii}/d$. The other scalar part is extracted out as

$$\tilde{\lambda}^S = -\frac{d}{d-1}\frac{\hat{k}_i\hat{k}_j}{k^2}\tilde{\lambda}_{\langle ij\rangle} = -\frac{d}{d-1}\frac{\hat{k}_i\hat{k}_j}{k^2}\left(\tilde{\lambda}_{ij} - \frac{1}{d}\delta_{ij}\tilde{\lambda}_{ii}\right), \tag{6}$$

where $\hat{k}_i \equiv k_i/k$, and the vector contribution turns out to be

$$\begin{aligned}\tilde{\lambda}_i^V &= -\frac{2i}{k^2}\left(k_j\tilde{\lambda}_{\langle ij\rangle} + \frac{d-1}{d}k_i k^2 \tilde{\lambda}^S\right) \\ &= -\frac{2i}{k^2}\left(k_j\tilde{\lambda}_{\langle ij\rangle} - k_i\hat{k}_p\hat{k}_q\tilde{\lambda}_{\langle pq\rangle}\right).\end{aligned} \tag{7}$$

Finally, the tensor part can thus be extracted from equation (5) as

$$\begin{aligned}\tilde{\lambda}_{ij}^T &= \tilde{\lambda}_{\langle ij\rangle} - \frac{d}{d-1}\hat{k}_{\langle i}\hat{k}_{j\rangle}\hat{k}_p\hat{k}_q\tilde{\lambda}_{\langle pq\rangle} \\ &\quad - \left[\left\{\hat{k}_i\hat{k}_p\tilde{\lambda}_{\langle jp\rangle} + (i\leftrightarrow j)\right\} - 2\hat{k}_i\hat{k}_j\hat{k}_r\hat{k}_s\tilde{\lambda}_{\langle rs\rangle}\right].\end{aligned} \tag{8}$$

The more conventional way to extract the TT part of the stress tensor is through the four-point projection operator $P_{ijlm}(\hat{k})$, defined as $P_{ijlm}(\hat{k}) \equiv \left[P_{il}P_{jm} - \frac{1}{2}P_{ij}P_{lm}\right](\hat{k})$ with $P_{ij}(\hat{k}) = \delta_{ij} - \hat{k}_i\hat{k}_j$, as is done, for example, in reference [60] (see their equation (22)). It can be shown in a straightforward way that the result of this operation gives the same expression as in equation (8). We now apply this formalism to the energy–momentum tensor for the magnetic and the plasma velocity fields.

2.2. SVT decomposition of magnetic stress

For a magnetic field $\mathbf{B}$, the stress tensor can be written as

$$\tau_{ij}(\mathbf{x}) = B_i(\mathbf{x})B_j(\mathbf{x}) - \frac{1}{2}\delta_{ij}B^2(\mathbf{x}), \tag{9}$$

where B_i are the spatial components of the three-dimensional vector $\mathbf{B}$. The magnetic field $\mathbf{B}$ is solenoidal, i.e., $\nabla \times \mathbf{B} = 0$. This tensor can be decomposed into its SVT contributions using equation (1),

$$\tau_{ij} = T\delta_{ij} + \nabla_{\langle i}\nabla_{j\rangle}\tau + \nabla_{(i}\bar{\tau}_{j)} + \bar{\tau}_{ij}, \tag{10}$$

where $\nabla_i\bar{\tau}_i = 0$, $\nabla_i\bar{\tau}_{ij} = \nabla_j\bar{\tau}_{ij} = 0$, and $\bar{\tau}_{ii} = 0$. An example is given in appendix B for a one-dimensional Beltrami field. The term proportional to the trace is $T = -B_iB_i/6 \equiv -B^2/6$, and the other scalar component is (see appendix A for the derivation of these expressions for general λ_{ij})

$$\tau = -\frac{1}{2}\int dV'\int dV''\frac{\nabla''^2\left[B^2(\mathbf{x}'')\right] - 3\nabla''_j B_i(\mathbf{x}'')\nabla''_i B_j(\mathbf{x}'')}{16\pi^2|\mathbf{x} - \mathbf{x}'||\mathbf{x}' - \mathbf{x}''|}, \tag{11}$$

and the vector contribution is

$$\bar{\tau}_j = \int dV'\frac{\nabla'_j\left\{B^2(\mathbf{x}') + 2\nabla'^2\tau(\mathbf{x}')\right\} - 3B_i(\mathbf{x}')\nabla'_i B_j(\mathbf{x}')}{6\pi|\mathbf{x} - \mathbf{x}'|}. \tag{12}$$

Note that the solenoidality of the magnetic field has been used to obtain equations (11) and (12). The tensor mode is then easily extracted by subtracting the scalar and vector contributions,

$$\bar{\tau}_{ij} = B_{\langle i}B_{j\rangle} - \nabla_{\langle i}\nabla_{j\rangle}\tau - \nabla_{(i}\bar{\tau}_{j)}, \tag{13}$$

where, as before, $B_{\langle i}B_{j\rangle} \equiv \left(B_iB_j - \delta_{ij}B^2/3\right)$. In Fourier space, the stress tensor in equation (9) becomes a convolution,

$$\tilde{\tau}_{ij}(\mathbf{k}) = \frac{1}{(2\pi)^3}\left(\tilde{B}_i \star \tilde{B}_j\right)(\mathbf{k}) \equiv \frac{1}{(2\pi)^3}\int \mathrm{d}^3\mathbf{p}\,\tilde{B}_i(\mathbf{p})\tilde{B}_j(\mathbf{k}-\mathbf{p}), \tag{14}$$

where $\tilde{B}_i(\mathbf{k})$ is the Fourier transform of $B_i(\mathbf{x})$, and we have omitted the isotropic term in equation (9). For the stress-tensor in equation (10), the expression analogous to equation (5) is,

$$\tilde{\tau}_{ij} = \tilde{T}\delta_{ij} - k_{\langle i}k_{j\rangle}\tilde{\tau}^S + ik_{(i}\tilde{\tau}^V_{j)} + \tilde{\tau}^T_{ij}, \tag{15}$$

with $k_i\tilde{\tau}^V_i = 0$, $k_i\tilde{\tau}^T_{ij} = k_j\tilde{\tau}^T_{ij} = 0$, and $\tilde{\tau}^T_{ii} = 0$. The term proportional to the trace is $\tilde{T} = (2\pi)^{-3}(\tilde{B}_s \star \tilde{B}_s)(\mathbf{k})/3$, while

$$\tilde{\tau}^S(\mathbf{k}) = -\frac{1}{(2\pi)^3}\frac{3}{2}\frac{\hat{k}_i\hat{k}_j}{k^2}\tilde{B}_{\langle i} \star \tilde{B}_{j\rangle}(\mathbf{k}), \tag{16}$$

where, continuing the spirit of using angle bracket notations, $\tilde{B}_{\langle i} \star \tilde{B}_{j\rangle}(\mathbf{k}) \equiv (\tilde{B}_i \star \tilde{B}_j)(\mathbf{k}) - \delta_{ij}(\tilde{B}_s \star \tilde{B}_s)(\mathbf{k})/3$. For clarity, we suppress the functional dependence on $\mathbf{k}$ henceforth. The vector contribution turns out to be

$$\tilde{\tau}^V_i = -\frac{2ik_j}{k^2}\left[\frac{1}{(2\pi)^3}\tilde{B}_{\langle i} \star \tilde{B}_{j\rangle} + k_{\langle i}k_{j\rangle}\tilde{\tau}^S\right], \tag{17}$$

and finally, the tensor part can thus be extracted as

$$\tilde{\tau}^T_{ij} = \frac{1}{(2\pi)^3}\tilde{B}_{\langle i} \star \tilde{B}_{j\rangle} + k_{\langle i}k_{j\rangle}\tilde{\tau}^S - ik_{(i}\tilde{\tau}^V_{j)}. \tag{18}$$

2.3. SVT decomposition of kinetic stress

For a fluid with velocity $\mathbf{u}$, the stress tensor analogous to equation (9) can be written as

$$\sigma_{ij}(\mathbf{x}) = w\gamma^2 u_i u_j - p\delta_{ij}, \tag{19}$$

where $w = p + \rho$ is the enthalpy[14], p and ρ are the pressure and density of the fluid respectively, $\gamma = (1 - u^2)^{-1/2}$ is the Lorentz factor, and the spacetime dependence of all the fields are suppressed[15]. The SVT decomposition of this tensor, analogous to equation (10), can be written as

$$\sigma_{ij} = S\delta_{ij} + \nabla_{\langle i}\nabla_{j\rangle}\sigma + \nabla_{(i}\bar{\sigma}_{j)} + \bar{\sigma}_{ij}, \tag{20}$$

---

[14] In a magnetized plasma, an important quantity associated with the magnetic field is the *Alfvén velocity* $\mathbf{v}_A$ defined as $\mathbf{v}_A = \mathbf{B}/\sqrt{w}$.

[15] If we have a solenoidal flow, i.e., $\nabla \times \mathbf{u} = 0$, then the anisotropic stress tensor for the fluid velocity γu_i is analogous to that of magnetic fields.

and as before, $\nabla_i \bar{\sigma}_i = 0$, $\nabla_i \bar{\sigma}_{ij} = \nabla_j \bar{\sigma}_{ij} = 0$, and $\bar{\sigma}_{ii} = 0$. The mathematical details are more involved compared to the case of magnetic fields, since the velocity fields are allowed to have a longitudinal component as opposed to the case with magnetic fields. In addition, we consider non-relativistic fluid velocities ($\gamma \sim 1$) for simplicity of the expressions in the analytical results. However, this factor is reinstated in the numerical treatment. We omit the general expressions for the S, V, and T components of the stress tensor in real space, which are provided in appendix C.

The stress tensor can be written in k-space in a manner analogous to equation (14) as

$$\tilde{\sigma}_{ij}(\mathbf{k}) = \frac{1}{(2\pi)^6} \left((\tilde{p} + \tilde{\rho}) \star \tilde{u}_i \star \tilde{u}_j \right)(\mathbf{k}) - \tilde{p}(\mathbf{k}) \delta_{ij}$$

$$= \frac{1}{(2\pi)^6} \int \mathrm{d}^3 \mathbf{p} \int \mathrm{d}^3 \mathbf{q} \left[(\tilde{p} + \tilde{\rho})(\mathbf{p}) \tilde{u}_i(\mathbf{q}) \tilde{u}_j(\mathbf{k} - \mathbf{p} - \mathbf{q}) \right] - \tilde{p}(\mathbf{k}) \delta_{ij}. \quad (21)$$

This is again decomposed as,

$$\tilde{\sigma}_{ij} = \tilde{S} \delta_{ij} - k_{\langle i} k_{j \rangle} \tilde{\sigma}^S + i k_{(i} \tilde{\sigma}^V_{j)} + \tilde{\sigma}^T_{ij}, \quad (22)$$

where $k_i \tilde{\sigma}^V_i = 0$, $k_i \tilde{\sigma}^T_{ij} = 0$, and $\tilde{\sigma}^T_{ii} = 0$. $\tilde{S}$ is again proportional to the trace, $\tilde{S} = -\tilde{p}(\mathbf{k}) + (2\pi)^{-6}((\tilde{p} + \tilde{\rho}) \star \tilde{u}_i \star \tilde{u}_i)(\mathbf{k})/3$, and the other scalar part is

$$\tilde{\sigma}^S(\mathbf{k}) = -\frac{1}{(2\pi)^6} \frac{3}{2} \frac{\hat{k}_i \hat{k}_j}{k^2} (\tilde{p} + \tilde{\rho}) \star \tilde{u}_{\langle i} \star \tilde{u}_{j \rangle}(\mathbf{k}), \quad (23)$$

and as in equations (17) and (18), we have

$$\tilde{\sigma}^V_i = -\frac{2 i k_j}{k^2} \left[\frac{1}{(2\pi)^6} (\tilde{p} + \tilde{\rho}) \star \tilde{u}_{\langle i} \star \tilde{u}_{j \rangle} + k_{\langle i} k_{j \rangle} \tilde{\sigma}^S \right], \quad (24)$$

and,

$$\tilde{\sigma}^T_{ij} = \frac{1}{(2\pi)^3} (\tilde{p} + \tilde{\rho}) \star \tilde{u}_{\langle i} \star \tilde{u}_{j \rangle} + k_{\langle i} k_{j \rangle} \tilde{\sigma}^S - i k_{(i} \tilde{S}^V_{j)}. \quad (25)$$

2.4. Modeling of turbulent sources

As mentioned above, the primordial plasma that generates the GWs is highly turbulent, and contains magnetic fields. It is therefore essential to study the MHD evolution of the plasma and understand the various kinds of turbulent initial conditions. The purpose of this subsection is to provide an elementary background of MHD turbulence, in preparation for the numerical results discussed in section 3.

The primordial plasma is described in a spatially flat, expanding, isotropic, and homogeneous Universe, characterized by the Friedmann–Lemaître–Robertson–Walker (FLRW) metric tensor, $\mathrm{d}s^2 = -a^2(\mathrm{d}t^2 + \delta_{ij}\mathrm{d}x_i\mathrm{d}x_j)$, where $\mathbf{x}$ are the comoving coordinates, t is the conformal time, and a is the scale factor. We consider turbulent sources with subrelativistic bulk velocities, such that the Lorentz factor can be expanded up to second order, $\gamma^2 \sim 1 + (v/c)^2$, and use the relativistic equation of state, $p = \rho c^2/3$, which is appropriate to describe a plasma dominated by massless particles. The resulting MHD equations are similar to those in flat spacetime after rescaling the magnetic fields, the energy, density and the spacetime coordinates to comoving variables and conformal time [44]. We consider the energy density in the turbulence to be below 10% of the total energy density, which is consistent with the assumption

of subrelativistic bulk velocities. The upper limit for a magnetic energy density of 10% of the energy densities of additional relativistic components is required based on big bang nucleosynthesis bounds on the observed abundance of light elements [61]. On the other hand, for kinetic turbulence, we defer the extension to relativistic velocities to future work. It should be said, however, that important phenomena in MHD turbulence such as inverse cascading are similarly reproduced both in relativistic [62] and nonrelativistic [63] simulations. Regarding GW production, the assumption of subrelativistic bulk velocities is justified, since it has been shown that neglecting the effect of thermal dissipation induced by shocks in the highly relativistic regime leads to an underestimation of the resulting GW signal; see reference [34].

Turbulent flows are characterized by the magnetic and fluid Reynolds numbers, $\mathrm{Re_M}$ and Re respectively, defined as

$$\mathrm{Re_M} \equiv \frac{vL}{\eta}, \qquad \mathrm{Re} \equiv \frac{vL}{\nu}, \tag{26}$$

for a typical fluid velocity v on the length scale L, with η and ν being the magnetic diffusivity and kinematic viscosity respectively. $\mathrm{Re_M}$ characterizes the relative importance of the diffusion term over the induction term, while Re tells us about the importance of the nonlinear velocity term relative to the viscous dissipation term.

In the early Universe, the viscosity and magnetic diffusivity are very small, leading to a very large value of the Reynolds numbers [43]. Under such conditions, numerical MHD simulations in an expanding Universe have demonstrated the occurrence of a direct cascade from larger to smaller scales, indicating the presence of turbulence; see reference [44] for pioneering work.

In MHD simulations, one generally studies the evolution of the energy spectra $E_i(k)$ of the velocity and magnetic fields, for $i = K, M$ respectively (these energy spectra are defined such that the mean energy density $\mathcal{E}_i$ is given by $\mathcal{E}_i = \int \mathrm{d}k\, E_i(k)$). In a turbulent medium, the energy spectra have a range of scales where the spectral shape is given by the Kolmogorov spectrum, i.e., $E_i(k) \propto k^{-5/3}$—this is called the inertial subrange; see [64] for a review. Scales smaller than the inertial range are dominated by viscous eddies, while larger scales have energy carrying eddies. Turbulence involves nonlinear dynamics, which leads to an energy cascade whereby energy is transferred from larger to smaller scales (direct cascade) or vice versa (inverse cascade). The latter, for example, is interesting in the context of evolution of PMFs, since it can explain the presence of magnetic fields correlated at sufficiently large scales in the Universe after they evolve through MHD evolution of the plasma.

The physics governing the MHD evolution of the magnetic and velocity fields of the plasma affects the instantaneous decay exponents of the mean energies. For example, if we have helical magnetic fields in a highly conducting plasma, magnetic helicity is conserved throughout the evolution; in that case, magnetic energy decays with time t as $\mathcal{E}_M(t) \propto t^{-2/3}$. On the other hand, for non-helical fields, one has $\mathcal{E}_M(t) \propto t^{-1}$. The correlation length of the turbulence, ξ_M, which is defined as a weighted average over the spectrum as $\xi_M = \mathcal{E}_i^{-1} \int \mathrm{d}k\, k^{-1} E_i(k)$, tends to increase in a corresponding fashion. The increase is fastest for helical turbulence, where $\xi_M \propto t^{2/3}$, and is slower for nonhelical turbulence, where $\xi_M \propto t^{1/2}$ [65]. This can have a noticeable effect on the resulting GW production [10].

3. Numerical SVT decomposition of the stress tensor

3.1. Numerical modeling setup

In the following, we present the results of a numerical SVT decomposition of the stress tensor. We consider four distinct types of isotropic hydrodynamic and MHD turbulence similar to

Table 1. Summary of the runs discussed in the paper.

Run	i	k_*	$\mathcal{E}_i^{\max}$	σ	Wave	$\mathcal{E}_{\mathrm{GW}}^{\mathrm{sat}}$	$\nu\,(=\eta)$	f_0	q
A	Ka	600	3.8×10^{-3}	0	Expan	1.5×10^{-8}	10^{-6}	1	19
B	Ka	600	2.4×10^{-3}	0	Plane	1.6×10^{-8}	2×10^{-7}	2×10^{-3}	32
C	Kv	600	8.0×10^{-3}	0	Plane	4.5×10^{-9}	2×10^{-7}	4×10^{-1}	4.3
D	Kv	600	1.1×10^{-2}	1	Plane	6.3×10^{-9}	2×10^{-7}	4×10^{-1}	5.0
E	Mv	600	5.7×10^{-3}	0	Plane	1.5×10^{-9}	2×10^{-7}	6×10^{-4}	4.1
F	Mv	600	1.7×10^{-2}	1	Plane	5.1×10^{-9}	2×10^{-7}	6×10^{-4}	2.5
G	Ka	2	4.2×10^{-2}	0	Plane	8.3×10^{-4}	2×10^{-2}	7×10^{-1}	1.4
H	Kv	2	4.7×10^{-2}	0	Plane	1.1×10^{-3}	1×10^{-2}	4×10^{-1}	1.4

those considered in recent numerical studies of GW production [10, 66]. The goal of those studies was to determine the form and amplitude of the GW spectra from numerical simulations of hydrodynamic and MHD turbulence. It was found that the efficiency of converting kinetic and magnetic energies into GW energy can be very different for different types of flows. The question therefore arises, whether this difference can be related to differences in the associated SVT decomposition. These flows are distinguished by different types of forcing; a summary is given in table 1.

The forcing energy is injected at wave numbers around k_*, which we arrange to be six times larger than the smallest wavenumber $k_1 = 2\pi/L$ in our triply-periodic computational domain of side length L. This forcing term is added to model the kinetic energy injection produced by different mechanisms that lead to turbulence generation during the early Universe. Some examples include the expansion and collision of bubbles during first-order phase transitions [11] or sound wave production due to scalar field perturbations [52]. Additionally, we model magnetic field generation in a similar way by injecting energy at a characteristic scale that depends on the magnetogenesis scenario; see reference [56] for a recent review. Axion-driven magnetogenesis can also induce turbulence at the QCD scale, and does not require the phase transition to be of first-order; see, e.g., reference [67]. Another possibility is to consider pre-existing (for example, inflationary) magnetic fields [68]. For most of the cases, we choose $k_1 = 100H_*$, and in two cases, we use $k_1 = 0.3H_*$). Energy is dissipated through a Laplacian diffusion operator with coefficients ν and η for the viscosity and the magnetic diffusivity, which act on the smallest resolved length scales. We use conformal time normalized to the Hubble time at the time of source initiation H_*^{-1}, which corresponds to $t = 1$ in our units. Following the recent work of reference [10], we apply a forcing term (in the momentum equation or in the induction equation for kinetic or magnetic turbulence, respectively) for one Hubble time until $t = 2$. The forcing has an initial stage $1 < t < 2$ when the forcing term is present, an intermediate stage $2 < t < 3$ when it decreases linearly, and a final stage $t > 3$ when it is absent. The forcing is random and applied at each time step. This allows to sustain stationary turbulence for a finite time during the intermediate stage, which leads to freely decaying turbulence in the final stage. For Run A, we apply forcing in the form of spherical expansion waves through the gradients of randomly placed Gaussians with amplitude f_0 [69], which are irrotational, i.e., curl-free. This case was also studied in reference [66], and is similar to their Run ac1, except that in their case the forcing was only applied until $t = 1.1$, and the intermediate stage is not considered. In Run B, we also apply irrotational forcing, but in the form of plane waves, again with amplitude f_0. The remaining four runs also have plane wave forcings, but are all vortical, calculated as a curl of a randomly oriented vector with amplitude f_0 and can have helicity, which is quantified by the parameter $\sigma \in [0, 1]$. Run C has nonhelical forcing, while Run D has a helical forcing. Runs E and F have magnetic fields and the forcing is applied in the induction equation, again
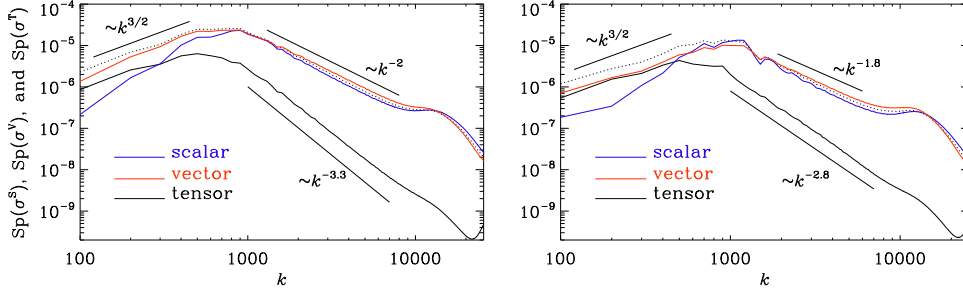
Figure 1. SVT decomposition for Runs A (left) and B (right) for irrotational turbulence produced by spherical expansion waves and plane wave forcing, respectively.
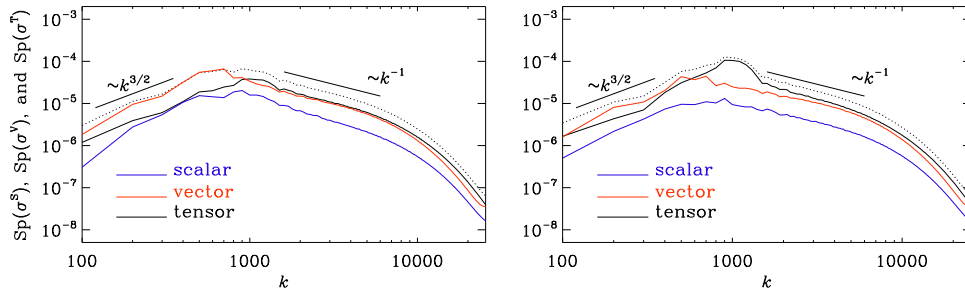
first without helicity (Run E) and with helicity (Run F). In Runs G and H, forcing is applied at small k ($k_* = 2$) during a time interval $1 \leqslant t \leqslant 2$, using either vortical (Run G) or irrotational (Run H) forcing. In all cases, we present the results of the SVT decomposition in the form of power spectra per linear wave number interval for the projected part of the stress tensor. The efficiency of GW production will be related to the contribution by the tensor mode with respect to the scalar and vector modes of the turbulent source. The energy injection wave numbers are $k = k_* \equiv 600$ (Runs A–F) and 2 (Runs G and H). The resulting spectra of the stress peak at $k = 2k_* \approx 1200$ and 4, respectively. Note that we have used normalized wave numbers k such that $k = 1$ corresponds to the Hubble scale H_*^{-1} at the time of generation.

3.2. Comparison for acoustic and vortical turbulence

In table 1, we list the maximum kinetic or magnetic energies $\mathcal{E}_i^{\mathrm{max}}$, where $i =$ Ka and Kv refer to kinetic energy densities for acoustic and vortical turbulence, and Mv for magnetic energy densities, where the turbulence is also vortical. These values are normalized by the radiation energy, just like the resulting GW energy, $\mathcal{E}_{\mathrm{GW}}^{\mathrm{sat}}$, which refers to the GW energy averaged over oscillations around the saturated stationary value. In the earlier work of reference [66], the saturation GW energy $\mathcal{E}_{\mathrm{GW}}^{\mathrm{sat}}$ was found to be proportional to the square of the ratio $\mathcal{E}_i^{\mathrm{max}}/k_*$. To characterize the efficiency in GW energy conversion, we quote in table 1 the factor $q = k_* (\mathcal{E}_{\mathrm{GW}}^{\mathrm{sat}})^{1/2}/\mathcal{E}_i^{\mathrm{max}}$. In reference [66], the values of q were found to be between one and ten, but here we find even larger values.

We begin with the case of acoustic turbulence in Runs A and B. This type of turbulence is unusual in that it processes very little vorticity. In figure 1, we show the power spectra of the projected stress tensor for acoustic turbulence, which always has zero helicity. The spectrum has a subinertial range proportional to $k^{3/2}$ and an inertial range which is proportional to k^{-2} for Run A and proportional to $k^{-1.8}$ for Run B, similar to what is expected for acoustic turbulence [70]. The scalar and vector components dominate over the tensor components at almost all wave numbers, although the scalar component becomes smaller than the tensor component at small wave numbers ($k < 400$). In addition, at small wave numbers, the vector components dominate over the scalar component.

The situation is quite different for vortical turbulence. We consider here cases without kinetic helicity (Run C) and with kinetic helicity (Run D). These two runs are similar in that they have a much shallower inertial range spectrum proportional to k^{-1}. In addition, we also consider two cases with magnetic fields, which are driven by an electromotive force. The functional form is the same as for the forcing in the momentum equation, but the amplitude factor f_0 tends to be much smaller while still leading to comparable stresses. This is a consequence

Figure 2. SVT decomposition for Runs C (left) and D (right) for vortical hydrodynamic turbulence without and with helicity, respectively.

of this forcing occurring underneath the curl of the induction equation. Run E has null magnetic helicity and Run F has maximum magnetic helicity; see figure 3. In these two cases, we find a somewhat steeper inertial range spectrum proportional to $k^{-5/3}$, but for Run F there is a clear uprise of the spectrum at low wavenumber, which is likely a consequence of an inverse cascade; see also [54] for hydromagnetic decay simulations showing inverse cascading. Those cases are rather similar in that now the tensor component is dominant; see figure 3.

As in the case of acoustic turbulence, the vector mode dominates over the scalar mode at the largest length scales ($k < 400$), with Run F being the exception (where the vector and scalar modes are comparable, and both much smaller than the tensor mode). For vortical hydrodynamic turbulence, the tensor and vector modes are comparable in the inertial range, while for magnetic turbulence the tensor mode dominates over this regime. Hence, in the magnetic turbulence case, the spectrum of the total unprojected stress tensor agrees surprisingly well with that of the tensor mode (for all k in the helical case, and at large k for the non-helical case), so the computational effort for doing such a projection could potentially be ignored in a first approximation, as was done in references [71, 72]. This is, however, not the case for acoustic turbulence, where the projection is essential.

It is worth noting that all spectra of figures 1–3 show a subinertial range proportional to k or $k^{3/2}$, which is shallower than the generic k^2 spectrum. In the present case, the subinertial range is not long enough to make strong claims, but it is useful to recall that deviations from a k^2 spectrum of the stress have been found when there are departures from Gaussianity of the underlying magnetic or velocity fields [73]. Although the departures from Gaussianity may not yet be very strong in the present simulations, it is worth noting that real astrophysical magnetic fields have much larger magnetic Reynolds numbers and may well lead to much more significant departures.

3.3. On the relative GW strength for acoustic and vortical turbulence

In this connection, it is interesting to note that the apparent strength of GWs for acoustic turbulence cannot straightforwardly be explained by the SVT decomposition. If there was such a connection, one would have expected the GW energy to be less for acoustic turbulence than for vortical turbulence, because the tensor mode (i.e., the actual source for the GWs) is weaker there. However, this is not the case [66]. We must therefore conclude that this difference between acoustic and vortical turbulence is explained by other factors, most likely the detailed aspects of the temporal variation of the stress. In fact, to drive GWs, the temporal stress frequency must be close to the frequency of light at each spatial Fourier mode and it seems plausible that this is more easily satisfied for acoustic turbulence. It can be argued that
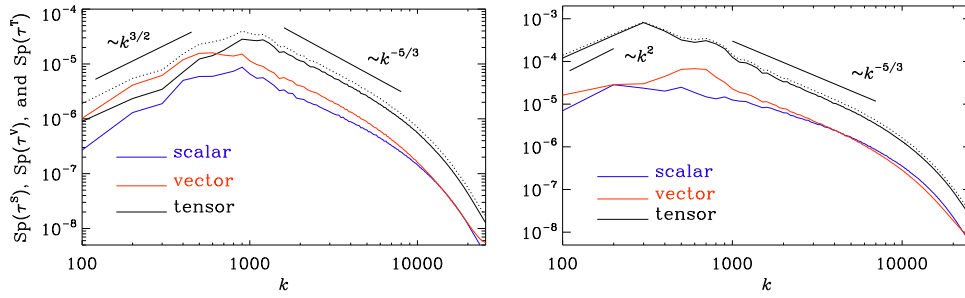
Figure 3. SVT decomposition for Runs E (left) and F (right) with magnetic forcing without and with helicity, respectively.
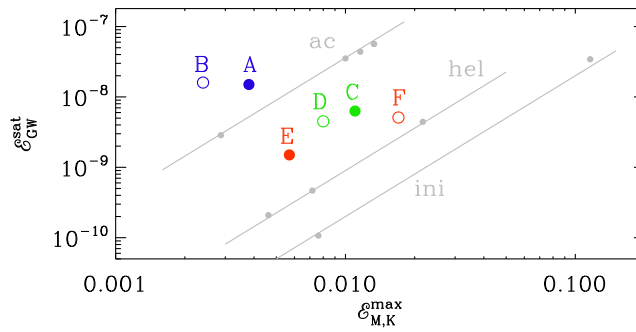

Figure 4. Positions of Runs A–F in a diagram showing $\mathcal{E}_{GW}^{sat}$ versus $\mathcal{E}_{M}^{max}$, For orientation the data points of the reference [66] are shown as gray symbols for acoustic (ac), helical (hel), initialized (ini) turbulence.

only the parallel component of the perturbations in magnetic fields contributes to the energy spectrum of the stress tensor of B^2 sourcing the GWs. Thus the acoustic modes of turbulence are more efficient in transferring energy to the GWs than the vortical modes, and thus GWs sourced by acoustic turbulence carry more energy compared to those by vortical turbulence.

In figure 4 we show the positions of Runs A–F in a $\mathcal{E}_{GW}^{sat}$ versus $\mathcal{E}_{M}^{max}$ diagram. For orientation, we also show the old data points from the reference [66]. We see that the new acoustic or irrotational turbulence simulations are now even slightly more efficient in driving GWs: Run B has not only the smallest kinetic energy of all the runs, but it also has a relatively large GW energy.

Larger GW energies can be obtained by decreasing k_*. In figure 5, we show the results for $k_* = 2$ and compare vortical and irrotational hydrodynamic forcings. Similarly to the cases with larger k_*, we see, again, that the tensor mode of acoustic turbulence is weaker (second panel of figure 5), but this is only true of the initial range, which contributes little to the total GW energy production. Most of the GW energy comes from wave numbers k below the peak, and there the tensor mode is, similarly to the cases with larger k_*, the largest (left panel of figure 5 around the peak, and right panel for low k) or, at least comparable to the vector mode, which is the largest (left panel of figure 5 for low k).
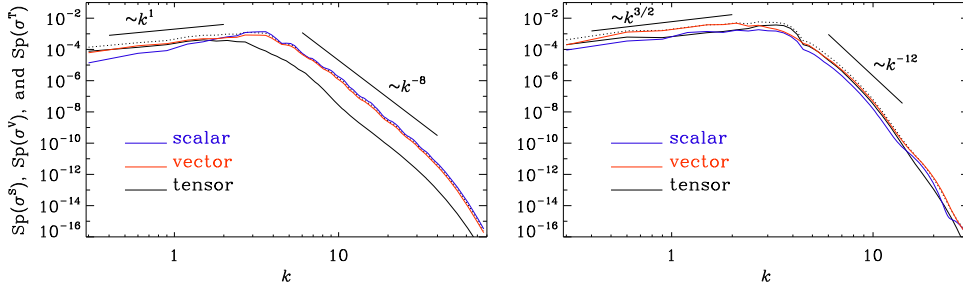
Figure 5. SVT decomposition for Runs E (left) and F (right) with $k_* = 2$ using irrotational and vortical forcings, respectively.

4. Relation between stress and strain spectra

4.1. GW equation for the radiation dominated epoch

In this section, we connect the observable quantities related to GWs to properties of the source obtained in the previous section. GWs are considered to be small tensor perturbations over the FLRW metric, and the dynamics of these GWs is given by the linearized Einstein equations. The perturbed metric is taken to be,

$$\mathrm{d}s^2 = -\mathrm{d}t_\mathrm{P}^2 + a^2(t_\mathrm{P})[\delta_{ij} + h_{ij,\mathrm{P}}(\mathbf{x}, t)]\mathrm{d}x_i\,\mathrm{d}x_j, \qquad (27)$$

where $\mathbf{x}$ are the comoving coordinates, t_P is the physical time, $a(t_\mathrm{P})$ is the scale factor of the Universe, and $h_{ij,\mathrm{P}}$ are the physical strains. The equation governing the evolution of these GWs is given by [58, 59],

$$\left[\frac{\partial^2}{\partial t_\mathrm{P}^2} + 3H(t_\mathrm{P})\frac{\partial}{\partial t_\mathrm{P}} - \frac{\nabla^2}{a^2}\right] h_{ij,\mathrm{P}}(\mathbf{x}, t_\mathrm{P}) = 16\pi G T_{ij,\mathrm{P}}^{\mathrm{TT}}(\mathbf{x}, t_\mathrm{P}), \qquad (28)$$

where G is Newton's constant, $H(t_\mathrm{P}) = \mathrm{d}a/(a\mathrm{d}t_\mathrm{P})$ is the Hubble rate, $T_{ij,\mathrm{P}}^{\mathrm{TT}}$ is the *physical* stress tensor, the superscript $^{\mathrm{TT}}$ denotes the transverse and traceless projection, and ∇ signifies derivatives with respect to the comoving coordinates $\mathbf{x}$.

The energy density in the magnetic fields and plasma velocity dilutes with the expansion of the Universe, and to scale out the effects of this expansion, we need to express the GW equation in terms of comoving stress tensor $T_{ij} = a^4 T_{ij,\mathrm{P}}$, the scaled strain $h_{ij} = ah_{ij,\mathrm{P}}$, and the conformal time t defined as $\mathrm{d}t_\mathrm{P} = a\mathrm{d}t$. Also in the radiation dominated epoch, the scale factor is linear in conformal time, and the damping term in the above equation vanishes. Equation (28) can then be expressed as

$$h_{ij}'' - \nabla^2 h_{ij} = \frac{16\pi G}{a} T_{ij}^{\mathrm{TT}}(\mathbf{x}, t), \qquad (29)$$

where the primes denote derivatives with respect to the conformal time t. The analytic solution of the GW equation is discussed in several references; see, for example, references [46, 71]. The full numerical solution for a turbulent source is also discussed in references [66, 74].

The four-dimensional power spectrum $H_{ijlm}(\mathbf{k}, t, \tau)$ of the energy density tensor is defined as

$$\frac{1}{w^2}\left\langle \tilde{T}_{ij}^*(\mathbf{k}, t)\tilde{T}_{lm}(\mathbf{k}', t + \tau)\right\rangle = (2\pi)^3\delta^3(\mathbf{k} - \mathbf{k}')H_{ijlm}(\mathbf{k}, t, \tau), \qquad (30)$$

where $\tilde{T}_{ij}(\mathbf{k}, t)$ is the Fourier transform of $T_{ij}(\mathbf{x}, t)$, we have used the reality condition $\tilde{T}_{ij}(-\mathbf{k}, t) = \tilde{T}_{ij}^*(\mathbf{k}, t)$. As mentioned previously, $w \equiv \rho + p$ is the enthalpy density of the primordial plasma, where ρ and p being the energy density and the pressure of the primordial plasma, and all quantities are comoving.

In the standard framework there are two degrees of freedom for h_{ij} (a 3×3 tensor has nine components, the symmetry condition $h_{ij} = h_{ji}$ leaves six degrees of freedom, the transverse nature of GWs, i.e., $k_i h^{ij} = 0$, reduces that to 3, while the traceless condition $h_{ii} = 0$ further reduces the total number of the degrees of freedom to 2) that correspond to two possible states of GWs polarization. In the case of a parity even source, these two states are equal to each other, while a parity odd sources generates circularly polarized GWs, where there is an excess of one state over the other. The circular polarization of GWs can be understood intuitively by working in the *circular polarization basis*, which can be constructed from the unit vector $\hat{\mathbf{k}}$, and two more unit vectors $\hat{\mathbf{e}}^1$ and $\hat{\mathbf{e}}^2$ which are perpendicular to $\hat{\mathbf{k}}$ and to each other. The basis is defined as [75]

$$\hat{e}_{ij}^{\mathrm{R,L}}(\hat{\mathbf{k}}) = -\frac{1}{2}(\hat{e}_1 \pm i\hat{e}_2)_i(\hat{e}_1 \pm i\hat{e}_2)_j. \tag{31}$$

It is easy to check that $(e_{ij}^{\mathrm{L}})^* = e_{ij}^{\mathrm{R}}$, and vice versa; and also that

$$\hat{e}_{ij}^{\mathrm{L}}(\hat{\mathbf{k}})\hat{e}_{ij}^{\mathrm{R}}(\hat{\mathbf{k}}) = 1, \tag{32}$$

$$\hat{e}_{ij}^{\mathrm{L}}(\hat{\mathbf{k}})\hat{e}_{ij}^{\mathrm{L}}(\hat{\mathbf{k}}) = \hat{e}_{ij}^{\mathrm{R}}(\hat{\mathbf{k}})\hat{e}_{ij}^{\mathrm{R}}(\hat{\mathbf{k}}) = \hat{k}_i \hat{e}_{ij}^{\mathrm{R,L}} = \delta_{ij}\hat{e}_{ij}^{\mathrm{R,L}} = 0. \tag{33}$$

The Fourier space stress tensor can now be decomposed into the left and right handed components,

$$\tilde{T}_{ij}(\mathbf{k}, t) = \tilde{T}_{\mathrm{L}}(\mathbf{k}, t)e_{ij}^{\mathrm{L}}(\hat{\mathbf{k}}) + \tilde{T}_{\mathrm{R}}(\mathbf{k}, t)e_{ij}^{\mathrm{R}}(\hat{\mathbf{k}}). \tag{34}$$

We can also construct symmetric and antisymmetric projectors [75],

$$\mathcal{S}_{ijlm}(\hat{\mathbf{k}}) \equiv \frac{1}{2}\left[e_{ij}^{\mathrm{L}}e_{lm}^{\mathrm{R}} + e_{ij}^{\mathrm{R}}e_{lm}^{\mathrm{L}}\right], \tag{35}$$

$$\mathcal{A}_{ijlm}(\hat{\mathbf{k}}) \equiv \frac{1}{2i}\left[e_{ij}^{\mathrm{R}}e_{lm}^{\mathrm{L}} - e_{ij}^{\mathrm{L}}e_{lm}^{\mathrm{R}}\right]. \tag{36}$$

These projection operators satisfy the properties that $\mathcal{S}_{ijlm}(\hat{\mathbf{k}})\mathcal{S}_{ijlm}(\hat{\mathbf{k}}) = \mathcal{A}_{ijlm}(\hat{\mathbf{k}})\mathcal{A}_{ijlm}(\hat{\mathbf{k}}) = 2$, and $\mathcal{S}_{ijlm}(\hat{\mathbf{k}})\mathcal{A}_{ijlm}(\hat{\mathbf{k}}) = 0$, and pick out respectively the symmetric and antisymmetric components of a fourth-order tensor.

The degree of polarization of the *source* can then be expressed as

$$\mathcal{P}_T(k, t) = \frac{T^{\mathcal{A}}(k, t)}{T^{\mathcal{S}}(k, t)}, \tag{37}$$

where

$$T^\alpha(k, t) = \frac{1}{2w^2}\int_{\Omega_k} d\Omega_k\, k^2 \int d^3\mathbf{k}'\, \alpha_{ijlm}(\hat{\mathbf{k}}) \left\langle \tilde{T}_{ij}^*(\mathbf{k}, t)\tilde{T}_{lm}(\mathbf{k}', t) \right\rangle, \tag{38}$$

with α denoting either $\mathcal{S}$ or $\mathcal{A}$.

In terms of the polarization components of equation (34), we can write

$$T^{\mathcal{S}}(k) = \frac{1}{2w^2}\int_{\Omega_k} d\Omega_k\, k^2 \int d^3\mathbf{k}' \left\langle \tilde{T}_{\mathrm{R}}^*(\mathbf{k})\tilde{T}_{\mathrm{R}}(\mathbf{k}') + \tilde{T}_{\mathrm{L}}^*(\mathbf{k})\tilde{T}_{\mathrm{L}}(\mathbf{k}') \right\rangle, \tag{39}$$

$$T^{\mathcal{A}}(k) = \frac{1}{2w^2} \int_{\Omega_k} d\Omega_k\, k^2 \int d^3\mathbf{k}' \left\langle \tilde{T}_R^*(\mathbf{k})\tilde{T}_R(\mathbf{k}') - \tilde{T}_L^*(\mathbf{k})\tilde{T}_L(\mathbf{k}') \right\rangle, \tag{40}$$

where the explicit t-dependence of the quantities in equation (39) is dropped for brevity. $\mathcal{P}_T(k,t)$ thus captures the relative inequality of power in the left and right handed components of the stress tensor. One can alternatively work in the *linear polarization basis*, where the physical meaning of the polarization degree of the source in terms of the corresponding components is not so straightforward. The definition of the basis, as well as the expressions analogous to those above are presented in appendix D. For more details about the linear and circular polarization bases, and the decomposition of the four-dimensional power spectrum into its symmetric and antisymmetric parts, see reference [75], where the stress tensor is sourced by magnetic fields. Notably, the analytical estimates for the polarization degree differ significantly from the numerical simulations due to the simplified treatment of the time-decorrelation functions and the neglect of different scaling laws for the energy density and helicity decays scalings; see reference [10] for more discussion.

Since GWs are sourced by the TT projected stress tensor, i.e., the tensor component $\bar{\lambda}_{ij}$ of the stress tensor (cf equation (1)), we built the four-dimensional power spectrum $H_{ijlm}(\mathbf{k},t,\tau)$ from this TT component and decomposed it into parity odd and even parts. It is of interest to see whether it is possible to ascribe a degree of polarization analogous to that in equation (37) to the scalar and vector components of the stress tensor. We defer a discussion of that to appendix E

4.2. Shell-integrated spectra

In a manner analogous to equation (30), we can form a four-dimensional power spectrum $Q_{ijlm}(\mathbf{k},t,\tau)$ from the time derivative of the strains in Fourier space

$$\frac{1}{32\pi G} \left\langle \dot{\tilde{h}}_{ij,P}^*(\mathbf{k},t)\dot{\tilde{h}}_{lm,P}(\mathbf{k}',t+\tau) \right\rangle = (2\pi)^3 \delta^3(\mathbf{k}-\mathbf{k}')Q_{ijlm}(\mathbf{k},t,\tau). \tag{41}$$

For more details on the fourth order correlation functions and their Fourier transforms, see reference [76].

The polarization degree of GWs is written as

$$\mathcal{P}_{GW}(k,t) = \frac{H_{GW}(k,t)}{E_{GW}(k,t)}, \tag{42}$$

where $E_{GW}(k,t)$ and $H_{GW}(k,t)$ are respectively the spectral GW energy density and the spectral GW helical energy density, obtained respectively by the application of the projection operators of equation (35) on the lhs of equation (41), in a way similar to equation (38).
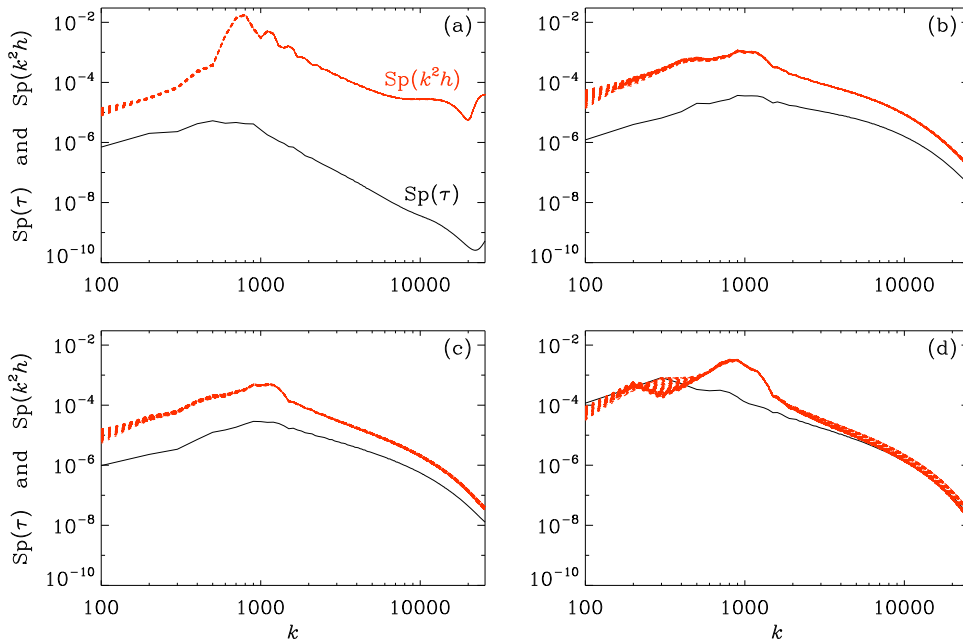
In the circular polarization basis, we get (dropping the explicit t-dependence)

$$E_{GW}(k) = \frac{1}{(2\pi)^6} \frac{1}{32\pi G} \int_{\Omega_k} d\Omega_k\, k^2 \int d^3\mathbf{k}' \left\langle \dot{\tilde{h}}_R^*(\mathbf{k})\dot{\tilde{h}}_R(\mathbf{k}') + \dot{\tilde{h}}_L^*(\mathbf{k})\dot{\tilde{h}}_L(\mathbf{k}') \right\rangle, \tag{43}$$

$$H_{GW}(k) = \frac{1}{(2\pi)^6} \frac{1}{32\pi G} \int_{\Omega_k} d\Omega_k\, k^2 \int d^3\mathbf{k}' \left\langle \dot{\tilde{h}}_R^*(\mathbf{k})\dot{\tilde{h}}_R(\mathbf{k}') - \dot{\tilde{h}}_L^*(\mathbf{k})\dot{\tilde{h}}_L(\mathbf{k}') \right\rangle, \tag{44}$$

where $\dot{\tilde{h}}_{ij,P}(\mathbf{k},t)$ is decomposed in the circular polarization basis,

$$\dot{\tilde{h}}_{ij}(\mathbf{k},t) = \dot{\tilde{h}}_L(\mathbf{k},t)e_{ij}^L(\hat{\mathbf{k}}) + \dot{\tilde{h}}_R(\mathbf{k},t)e_{ij}^R(\hat{\mathbf{k}}). \tag{45}$$

Figure 6. Spectra of stress (solid line at maximum) and strain (dotted lines for different times after the maximum) for Runs B, C, E, and F.

As expected, $\mathcal{P}_{\mathrm{GW}}(k,t)$ captures the relative inequality of power in the left and right handed components of the GW perturbations.

4.3. Numerical results for the strain and stress spectra

We now solve for the resulting GWs numerically using the approach described in references [66, 74]. Here we focus on a comparison of the results with irrotational plane wave (Run B) and vortical plane wave forcings without (Run C) and with (Run D) magnetic field, and with helicity (Run F). In each of the cases, we show the spectra of both the TT-projected stress of the magnetic (kinetic) fields $\bar{\tau}_{ij}$ ($\bar{\sigma}_{ij}$), and the strain h scaled with a k^2 factor. Here we denote the latter simply as $\mathrm{Sp}(k^2 h)$, but mean by this all of the components of the strain tensor. Likewise, we denote the stress spectrum by $\mathrm{Sp}(\tau)$, and mean by this the TT-projected stress tensor with the $16\pi G$ factor included, so that it would be equal to $\mathrm{Sp}(k^2 h)$, if the second conformal time derivative of the strain in equation (29) was absent. The result is shown in figure 6 for Runs B, C, E, and F.

We see from figure 6(d) that in the magnetic case with helicity, the spectra of $\mathrm{Sp}(k^2 h)$ and $\mathrm{Sp}(\tau)$ are in almost perfect agreement with each other at all wave numbers, except near $2k_*$. The situation changes when there is no helicity and $\mathrm{Sp}(k^2 h)$ is now slightly above $\mathrm{Sp}(\tau)$; see figure 6(c). The difference increases further when we compare with purely hydrodynamic cases (Run C); see figure 6(b). Particularly striking is a difference for irrotational turbulence, where we see significant differences between the two spectra at all wave numbers (Run B); see figure 6(a).

Our results suggest that, although there is a correspondence between $\mathrm{Sp}(k^2 h)$ and $\mathrm{Sp}(\tau)$, there can also be a significant departure and even a shift between them. Thus, even though the TT-projection of the stress has resulted in a significant decrease in the projected stress (see figure 1), the stress in the irrotational hydrodynamic cases have now other qualities that
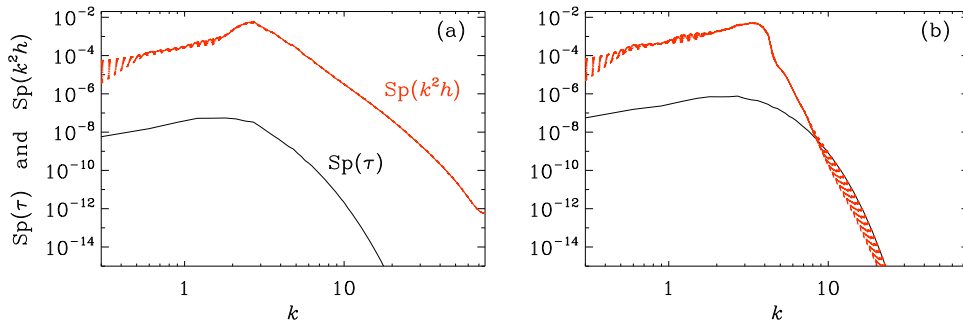
Figure 7. Spectra of stress (solid line at maximum) and strain (dotted lines for different times after the maximum) for Runs G and H.

make it more efficient for driving GWs. As already discussed above, this could be caused by larger power at larger temporal frequencies. This is supported by our findings that in the cases with the smallest efficiency (Run D), the two spectra are almost equal, i.e., $\mathrm{Sp}(\tau) \approx \mathrm{Sp}(k^2 h)$ (see figure 7).

### 4.4. Polarization spectra of stress and strain

It is common to define the degree of polarization in terms of the strains themselves, as opposed to our definition in terms of the time derivatives of the strains (see, e.g., equation (6) of reference [46]). It can be argued that these definitions are equivalent for GWs sourced by stationary turbulence, where one can apply the *aeroacoustic approximation*. For stationary turbulence, one can take the time derivatives out of the time averaging operation on the four-point correlation function of the stress tensor (see equation (12) of reference [71]). The same reasoning applies to the four-point correlation function of the GW strain, since the strains are expected to have the same statistical properties as the turbulent source. This means

$$\left\langle \dot{h}^{\mathrm{TT}}_{ij,\mathrm{P}}(\mathbf{x}, t)\dot{h}^{\mathrm{TT}}_{lm,\mathrm{P}}(\mathbf{x}+\boldsymbol{\xi}, t+\tau)\right\rangle_t = -\partial_t^2 \left\langle h^{\mathrm{TT}}_{ij,\mathrm{P}}(\mathbf{x}, t)h^{\mathrm{TT}}_{lm,\mathrm{P}}(\mathbf{x}+\boldsymbol{\xi}, t+\tau)\right\rangle_t, \tag{46}$$

where the subscript t is used to denote that the angle brackets now also include time averaging, in addition to the ensemble averaging. In frequency space, the time derivatives become factors of frequency, and cancel out when calculating the degree of polarization (see equation (42)).

Let us now discuss the degree of polarization of the source, $\mathcal{P}_T(k)$, and of the strain. $\mathcal{P}_h(k)$, from numerical simulations. In figures 8(a) and (b) we show $\mathcal{P}_T(k)$ for the source for the runs of reference [10] for kinetic and magnetic driving. The run names for the kinetically driven cases are K0, K01, K03, K05, and K1 for $\sigma = 0$, 0.1, 0.3, 0.5, and 1, respectively. The magnetically driven runs have analogous names M0, M01, M03, M05, and M1.

Remarkably, in the kinetically driven case, the polarization of the source never reaches 100%, and yet, the polarization of h does reach nearly 100%. This was already found in reference [10], and their results are convenient comparison also reproduced in figures 8(c) and (d). Furthermore, in the magnetically driven case, the source reaches nearly 100%, but not at the same wave number where the GWs become 100% polarized. Instead, maximum polarization happens here at the smallest scale.
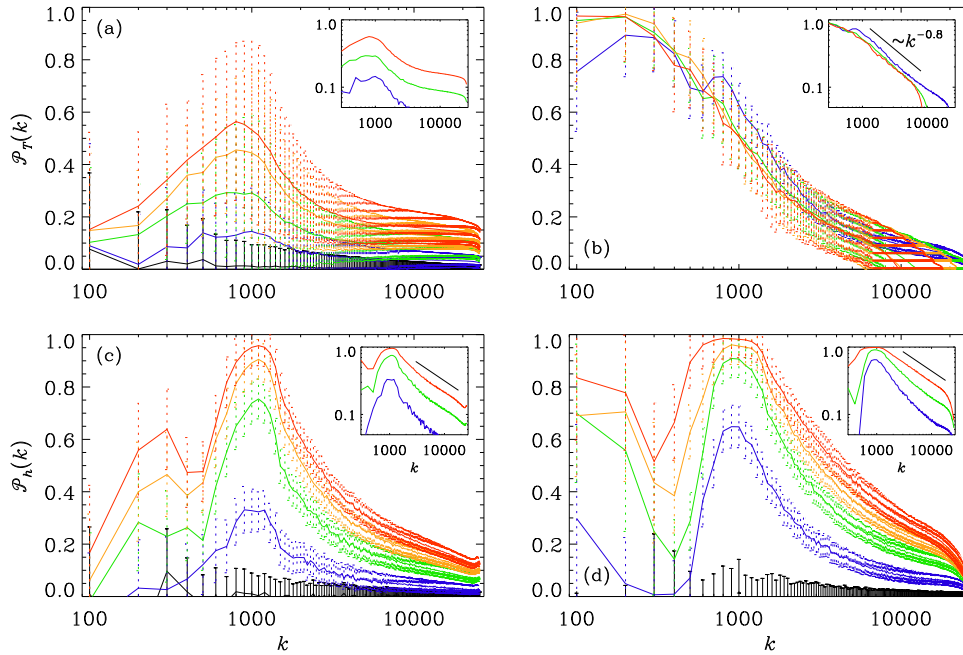
Figure 8. Degree of polarization of T^{TT} for (a) Runs K0, K01, K03, K05, and K1 of reference [10], and (b) their Runs M01, M03, M05, and M1, as well as the degree of polarization of h (c) for Runs K0, K01, K03, K05, and K1, and (d) for Runs M01, M03, M05, and M1. The inserts show the same, but in a double-logarithmic representation. For (b), the straight line has a slope of -0.8, while for (c) and (d) the two straight lines have a slope of -0.55.

5. Conclusions

We have computed the SVT decomposition for six different flows: kinetically and magnetically driven flows, with and without helicity, as well as two types of acoustically driven flows. In addition, we have considered two cases with significantly smaller forcing wave numbers. All our flows had a turbulent inertial range spectrum, as well as a subinertial range spectrum. However, significant differences can be seen in the relative strengths of scalar, vector, and tensor modes of the turbulent source. The largest contribution to the tensor mode comes from the flows in Runs E and F. Both are magnetically driven, although only one of them has helicity. In the presence of magnetic helicity (Run F), an inverse cascade emerges, which leads to an additional contribution to the tensor mode at small wave numbers. The scalar and vector modes of the turbulence stress are small and of comparable strengths in the helically driven case. Without helicity, however, the vector mode exceeds the scalar mode at small and intermediate length scales. For helically driven flows, there is no significant inverse cascade, and the tensor mode is no longer so dominant. Instead, tensor and vector modes are now of comparable strength. At smaller wave numbers, the vector mode does even become dominant.

For acoustically or irrotationally driven flows, the situation is drastically different in that the tensor mode is now comparatively weak, while scalar and vector modes are dominant and of similar strengths. Furthermore, there is very little difference between two fundamentally different realizations of acoustic turbulence: plane wave and spherical expansion wave forcings.

Both show a very strong 'bottleneck' effect, i.e., a shallower spectrum at high wave numbers, which was already found in reference [69]. Bottleneck effects are known to exist also for vortical turbulence [77], but they are not as strong [79]. The planar wave forcing was thought to be more similar to the vortical plane wave forcing, but this is not the case. Even though the acoustically driven flows have comparatively weak tensor modes, they are most effective in driving GWs. The reason for this higher efficiency of acoustic flows in generating GWs is not very well understood; but it might be interesting to note that at least in a gravitationally stratified fluid, maximum acoustic wave power output was found for flows with significant longitudinal modes compared to transverse ones [78]. The planar wave-driven acoustic flows are even slightly more effective (Run B, $q = 32$), than spherical expansion wave-driven flows (Run A, $q = 19$).

Given that the presence of helicity had no significant effect on the results of the SVT decomposition, it was of interest to look for differences in the degree of polarization of the source and the resulting GWs. The difference is indeed immense, but it results almost entirely from the inverse cascade, which is only possible in the magnetically driven case. In these cases, the degree of polarization of the source is virtually independent of the fractional helicity. This is probably because, even for weak magnetic helicity, inverse cascading is possible. At the driving scale, however, the degree of polarization is never close to 100%—neither in the magnetically driven cases, nor in the kinetically driven ones. In the latter, however, fractional helicity of the velocity does lead to a smaller fractional helicity of the stress. By contrast, in the magnetically driven cases, all spectra of the polarization degree are similar and they seem to be controlled by some kind of forward cascade from the largest scale downward to all smaller scales. This includes even the driving scale of the system, whose degree of polarization seems to be controlled by the stress on the largest scale of the domain.

Clearly, spectral power on the scale of the domain must be interpreted with care, because the intention of periodic box simulations is to represent an infinite and unbounded domain. The results will therefore be different if one considered a larger domain. It is conceivable, then, that inverse cascading also works in an infinitely extend domain, but, again, only on the scale of the domain will the polarization degree be close to maximum.

The work presented here will be important for identifying the nature of the turbulent motions in the early Universe once a GW signal from turbulent sources will be detected. More specifically, it can help to disentangle the turbulent conditions in the early Universe regarding the dependence on irrotational (longitudinal) and vortical (solenoidal) flows.

Data availability—the source code used for the simulations of this study, the Pencil Code, is freely available [80]. The simulation setups and the corresponding data are freely available from references [81, 82].

Acknowledgments

Data availability statement

The data that support the findings of this study are openly available at the following URL/DOI:
https://doi.org/10.5281/zenodo.4256906.

Appendix A. Helmholtz theorem and the real space SVT decomposition

The SVT decomposition is the most generalized way to decompose linearized perturbations
of a symmetric rank-2 tensor based on how these components transform under rotations. In
this formulation, the evolution equations for the scalar, vector, and tensor components of the
metric perturbations are decoupled from each other at the linear level. It is a more generalized
version of the Helmholtz decomposition where a vector is decomposed into divergence-free
and curl-free parts.

In section 2.1, we have provided the expressions for the SVT decomposition of a general
symmetric rank-2 tensor in momentum space. In this appendix, we show the corresponding
decomposition in real space.

The Helmholtz theorem states that any three-vector b_i can be decomposed into a scalar part
b and a vector part $\bar{b}_i$,

$$b_i = \nabla_i b + \bar{b}_i. \tag{A.1}$$

The first term on the rhs is curl-free and the second term is divergence-free, $\nabla_i \bar{b}_i = 0$. To extract
this latter part, we need to solve for b; we get the following condition on b,

$$\nabla^2 b = \nabla_i b_i(\mathbf{x}). \tag{A.2}$$

This corresponds to a Poisson's equation, whose general solution in three dimensions is

$$b = -\int dV' \frac{\nabla'_i b_i(\mathbf{x}')}{4\pi|\mathbf{x} - \mathbf{x}'|}, \tag{A.3}$$

where the prime on the ∇ indicates that the derivative is with respect to the components of $\mathbf{x}'$;
we thus get,

$$\bar{b}_i = b_i + \nabla_i \int dV' \frac{\nabla'_j b_j(\mathbf{x}')}{4\pi|\mathbf{x} - \mathbf{x}'|}. \tag{A.4}$$

Analogous to the case for vectors, we have SVT decomposition for tensors—any symmetric
rank-2 tensor $\lambda_{ij}(\mathbf{x})$ can be decomposed as in equation (1). Taking the trace of equation (1), we
get,

$$L = \frac{1}{d}\lambda_{ii}, \tag{A.5}$$

which allows us to rewrite equation (1), using the condensed notation $\lambda_{\langle ij\rangle} \equiv \lambda_{ij} - \delta_{ij}\lambda_{ss}/d$,

$$\lambda_{\langle ij\rangle} = \nabla_{\langle i}\nabla_{j\rangle}\lambda + \nabla_{(i}\bar{\lambda}_{j)} + \bar{\lambda}_{ij}. \tag{A.6}$$

Acting on this with ∇_i and then with ∇_j, we get,

$$\nabla_i\nabla_j\lambda_{\langle ij\rangle} = \frac{d-1}{d}\nabla^2\left(\nabla^2\lambda\right), \tag{A.7}$$

and thus, we can solve for λ, by solving the Poisson's equation (A.7) first for $\nabla^2\lambda$, and then for λ in d dimensions[16],

$$\lambda = \frac{d}{d-1}\frac{\Gamma^2\left(\frac{d}{2}-1\right)}{16\pi^d}\int \mathrm{d}V' \int \mathrm{d}V'' \frac{\nabla_i''\nabla_j''\lambda_{\langle ij\rangle}(\mathbf{x}'')}{|\mathbf{x}-\mathbf{x}'|^{d-2}|\mathbf{x}'-\mathbf{x}''|^{d-2}}. \tag{A.8}$$

To extract $\bar{\lambda}_i$, we insert this value of λ into equation (1) and act on it with ∇_j,

$$\nabla^2\bar{\lambda}_i = 2\nabla_j\lambda_{\langle ij\rangle} - \frac{2(d-1)}{d}\nabla_i\left(\nabla^2\lambda\right), \tag{A.9}$$

where λ is understood to be known from equation (A.8). Solving this,

$$\bar{\lambda}_i = -\frac{\Gamma\left(\frac{d}{2}-1\right)}{2\pi^{\frac{d}{2}}}\int \mathrm{d}V' \frac{\nabla_j'\lambda_{\langle ij\rangle}(\mathbf{x}') - (d-1)\nabla_i'\nabla'^2\lambda(\mathbf{x}')/d}{|\mathbf{x}-\mathbf{x}'|^{d-2}}. \tag{A.10}$$

Finally, the traceless, divergenceless part of the energy–momentum tensor is,

$$\begin{aligned}
\bar{\lambda}_{ij} = \lambda_{\langle ij\rangle} &- \frac{d}{d-1}\frac{\Gamma^2\left(\frac{d}{2}-1\right)}{16\pi^d}\nabla_{\langle i}\nabla_{j\rangle}\int \mathrm{d}V' \int \mathrm{d}V'' \frac{\nabla_m''\nabla_n''\lambda_{\langle mn\rangle}(\mathbf{x}'')}{|\mathbf{x}-\mathbf{x}'|^{d-2}|\mathbf{x}'-\mathbf{x}''|^{d-2}} \\
&+ \frac{\Gamma\left(\frac{d}{2}-1\right)}{4\pi^{\frac{d}{2}}}\int \mathrm{d}V' \\
&\cdot \left[\nabla_j \frac{\nabla_m'\lambda_{\langle im\rangle}(\mathbf{x}') + \frac{\Gamma^2\left(\frac{d}{2}-1\right)}{16\pi^d}\nabla_i'\nabla'^2\int \mathrm{d}V'' \int \mathrm{d}V''' \frac{\nabla_m'''\nabla_n'''\lambda_{\langle mn\rangle}(\mathbf{x}''')}{|\mathbf{x}'-\mathbf{x}''|^{d-2}|\mathbf{x}''-\mathbf{x}'''|^{d-2}}}{|\mathbf{x}-\mathbf{x}'|^{d-2}} \right. \\
&+ \left. (i\leftrightarrow j)\right]. \tag{A.11}
\end{aligned}$$

Appendix B. An example

It is instructive to consider an example for the formalism of section 2.2. For a Beltrami field, $\mathbf{B} = (0,\ \sin kx, \cos kx)$, we have

$$\tau_{ij} = \frac{1}{2}\begin{pmatrix} -1 & 0 & 0 \\ 0 & -\cos 2kx & \sin 2kx \\ 0 & \sin 2kx & \cos 2kx \end{pmatrix}. \tag{B.1}$$

One can easily verify that

$$\bar{\tau}_{ij} = \frac{1}{2}\begin{pmatrix} 0 & 0 & 0 \\ 0 & -\cos 2kx & \sin 2kx \\ 0 & \sin 2kx & \cos 2kx \end{pmatrix}, \tag{B.2}$$

is traceless and transverse. Using $\tau = (y^2 + z^2)/4$, we have $\nabla_{\langle i}\nabla_{j\rangle}\tau = \mathrm{diag}(-2,1,1)/6$. Next, using $T = -1/6$, we see that $T\delta_{ij} + \nabla_{\langle i}\nabla_{j\rangle}\tau = \mathrm{diag}(-1/2,0,0)$. Thus, following equation

---

[16] For notes on deriving the Green's function of ∇^2 in d dimensions see, for example, the discussion in https://tinyurl.com/knnm7bbc.

(10), we can write τ_{ij} as $T\delta_{ij} + \nabla_{\langle i}\nabla_{j\rangle}\tau + \nabla_{(i}\bar{\tau}_{j)} + \bar{\tau}_{ij}$ with $\bar{\tau}_j = 0$. The Beltrami field therefore has only a spatially periodic tensor mode, a spatially (unbounded) nonperiodic scalar mode, and no vector mode.

Appendix C. The SVT decomposition of the fluid stress tensor

In this section, we provide the expressions for the scalar, vector, and tensor components of the plasma velocity stress tensor of equation (19). As before, one gets the trace-term to be

$$S = -p + \frac{1}{3}w\gamma^2 u^2, \tag{C.1}$$

and we can then solve for σ,

$$\sigma = \frac{3}{32\pi^2}\int dV'\int dV''\frac{\nabla_i''\nabla_j''\left\{(p+\rho)(\mathbf{x}'')\gamma^2(\mathbf{x}'')u_{\langle i}u_{j\rangle}(\mathbf{x}'')\right\}}{|\mathbf{x}-\mathbf{x}'||\mathbf{x}'-\mathbf{x}''|}. \tag{C.2}$$

The vector part is also extracted in a straightforward manner,

$$\bar{\sigma}_i = -\frac{1}{2\pi}\int dV'\frac{\nabla_j'\left\{(p+\rho)(\mathbf{x}')\gamma^2(\mathbf{x}')u_{\langle i}u_{j\rangle}(\mathbf{x}')\right\} - 2\nabla_i'\nabla'^2\sigma(\mathbf{x}')/3}{|\mathbf{x}-\mathbf{x}'|}. \tag{C.3}$$

The tensor part finally comes out by subtracting the scalar and vector parts from the full tensor,

$$\bar{\sigma}_{ij} = w\gamma^2 u_{\langle i}u_{j\rangle} - \nabla_{\langle i}\nabla_{j\rangle}\sigma - \nabla_{(i}\bar{\sigma}_{j)}. \tag{C.4}$$

Appendix D. The linear polarization basis

In a manner similar to the circular polarization basis, one can also define the **linear polarization basis** [75],

$$e_{ij}^+(\hat{\mathbf{k}}) = e_i^1 e_j^1 - e_i^2 e_j^2, \qquad e_{ij}^\times(\hat{\mathbf{k}}) = e_i^1 e_j^2 + e_i^2 e_j^1, \tag{D.1}$$

which is orthogonal, but not normalized, and has the properties

$$e_{ij}^+(\hat{\mathbf{k}})e_{ij}^+(\hat{\mathbf{k}}) = e_{ij}^\times(\hat{\mathbf{k}})e_{ij}^\times(\hat{\mathbf{k}}) = 2, \qquad e_{ij}^+(\hat{\mathbf{k}})e_{ij}^\times(\hat{\mathbf{k}}) = 0. \tag{D.2}$$

In addition, the fact that $\hat{\mathbf{e}}^1$, $\hat{\mathbf{e}}^2$, and $\hat{\mathbf{k}}$ form a right-handed orthonormal basis leads to the relations

$$-\epsilon_{ipq}\hat{k}_p e_{qj}^\times(\hat{\mathbf{k}}) = e_{ij}^+(\hat{\mathbf{k}}), \qquad \epsilon_{ipq}\hat{k}_p e_{qj}^+(\hat{\mathbf{k}}) = e_{ij}^\times(\hat{\mathbf{k}}). \tag{D.3}$$

As in equation (34), we can decompose the stress tensor into $+$ and $\times$ polarization modes,

$$\tilde{T}_{ij}(\mathbf{k},t) = \tilde{T}_+(\mathbf{k},t)\,e_{ij}^+(\hat{\mathbf{k}}) + \tilde{T}_\times(\mathbf{k},t)\,e_{ij}^\times(\hat{\mathbf{k}}). \tag{D.4}$$

The projection operators of equation (35) can be written in this basis as

$$\mathcal{S}_{ijlm}(\hat{\mathbf{k}}) \equiv \frac{1}{2}\left[e_{ij}^+ e_{lm}^+(\hat{\mathbf{k}}) + e_{ij}^\times e_{lm}^\times(\hat{\mathbf{k}})\right], \tag{D.5}$$

$$\mathcal{A}_{ijlm}(\hat{\mathbf{k}}) \equiv \frac{1}{2}\left[e_{ij}^\times e_{lm}^+(\hat{\mathbf{k}}) - e_{ij}^+ e_{lm}^\times(\hat{\mathbf{k}})\right], \tag{D.6}$$

22

and the degree of polarization in of the source can be expressed with equation (37), where in terms of the components in the linear polarization basis,

$$T^S(k) = \frac{1}{w^2} \int_{\Omega_k} d\Omega_k \, k^2 \int d^3\mathbf{k}' \left\langle \tilde{T}^*_+(\mathbf{k})\tilde{T}_+(\mathbf{k}') + \tilde{T}^*_\times(\mathbf{k})\tilde{T}_\times(\mathbf{k}') \right\rangle, \tag{D.7}$$

$$T^A(k) = \frac{1}{w^2} \int_{\Omega_k} d\Omega_k \, k^2 \int d^3\mathbf{k}' \left\langle \tilde{T}^*_\times(\mathbf{k})\tilde{T}_+(\mathbf{k}') - \tilde{T}^*_+(\mathbf{k})\tilde{T}_\times(\mathbf{k}') \right\rangle, \tag{D.8}$$

where the explicit t-dependence is dropped as in equation (39). Similarly, the spectral energy densities of GWs is written in this basis as (again dropping explicit t-dependence)

$$E_{\mathrm{GW}}(k) = \frac{1}{(2\pi)^6} \frac{1}{16\pi G} \int_{\Omega_k} d\Omega_k \, k^2 \int d^3\mathbf{k}' \left\langle \dot{\tilde{h}}^*_+(\mathbf{k})\dot{\tilde{h}}_+(\mathbf{k}') + \dot{\tilde{h}}^*_\times(\mathbf{k})\dot{\tilde{h}}_\times(\mathbf{k}') \right\rangle, \tag{D.9}$$

$$H_{\mathrm{GW}}(k) = \frac{1}{(2\pi)^6} \frac{1}{16\pi G} \int_{\Omega_k} d\Omega_k \, k^2 \int d^3\mathbf{k}' \left\langle \dot{\tilde{h}}^*_\times(\mathbf{k})\dot{\tilde{h}}_+(\mathbf{k}') - \dot{\tilde{h}}^*_+(\mathbf{k})\dot{\tilde{h}}_\times(\mathbf{k}') \right\rangle. \tag{D.10}$$

Appendix E. Polarization of the *S* and *V* components of the stress tensor

One can define a four-dimensional power spectrum analogous to that in equation (30) from the scalar and vector components of the general stress tensor λ_{ij} of equation (1). Indeed using equation (5), we can write

$$\frac{1}{w^2} \left\langle k_{\langle i}k_{j\rangle}\tilde{\lambda}^{*S}(\mathbf{k},t) \cdot k'_{\langle l}k'_{m\rangle}\tilde{\lambda}^S(\mathbf{k}',t+\tau) \right\rangle \equiv (2\pi)^3\delta^3(\mathbf{k}-\mathbf{k}')H^S_{ijlm}(\mathbf{k},t,\tau), \tag{E.1}$$

and

$$\frac{1}{w^2} \left\langle k_{\langle i}\tilde{\lambda}^{*V}_{j\rangle}(\mathbf{k},t) \cdot k'_{\langle l}\tilde{\lambda}^V_{m\rangle}(\mathbf{k}',t+\tau) \right\rangle \equiv (2\pi)^3\delta^3\left(\mathbf{k}-\mathbf{k}'\right)H^V_{ijlm}(\mathbf{k},t,\tau). \tag{E.2}$$

One can define antisymmetric analogs of these,

$$\mathscr{H}^{S,V}_{ijlm}(\mathbf{k},t,\tau) \equiv -\epsilon_{ipq}\hat{k}_p H^{S,V}_{qjlm}(\mathbf{k},t,\tau), \tag{E.3}$$

with respective 'degrees of polarization' defined as

$$\mathcal{P}^{S,V}_T(k,t) = \frac{\int_\Omega d\Omega \, k^2 \, \mathscr{H}^{S,V}_{ijij}(\mathbf{k},t,0)}{\int_\Omega d\Omega \, k^2 H^{S,V}_{ijij}(\mathbf{k},t,0)}. \tag{E.4}$$

It follows in a straightforward manner from equation (E.1) that $\mathscr{H}^S_{ijij}(\mathbf{k},t,0) = 0$, and there is no polarization associated with the scalar part of the stress tensor, as would be intuitively expected. However, $\mathscr{H}^V_{ijij}(\mathbf{k},t,0)$ does not necessarily vanish, and one can associate a degree of polarization with the vector component of the source.

ORCID iDs

Axel Brandenburg ⓘ https://orcid.org/0000-0002-7304-021X
Grigol Gogoberidze ⓘ https://orcid.org/0000-0002-0506-333X
Tina Kahniashvili ⓘ https://orcid.org/0000-0003-0217-9852
Sayan Mandal ⓘ https://orcid.org/0000-0003-3129-5799
Alberto Roper Pol ⓘ https://orcid.org/0000-0003-4979-4430

References

[1] Maggiore M 2018 *Gravitational Waves* (*Astrophysics and Cosmology* vol 2) (Oxford: Oxford University Press)

[2] Durrer R and Kahniashvili T 1998 CMB anisotropies caused by gravitational waves: a parameter study *Helv. Phys. Acta* **71** 445

[3] Weinberg S 2004 Damping of tensor modes in cosmology *Phys. Rev.* D **69** 023503

[4] Mangilli A, Bartolo N, Matarrese S and Riotto A 2008 The impact of cosmic neutrinos on the gravitational-wave background *Phys. Rev.* D **78** 083517

[5] Lattanzi M, Benini R and Montani G 2010 A possible signature of cosmic neutrino decoupling in the nHz region of the spectrum of primordial gravitational waves *Class. Quantum Grav.* **27** 194008

[6] Stefanek B A and Repko W W 2013 Analytic description of the damping of gravitational waves by free streaming neutrinos *Phys. Rev.* D **88** 083536

[7] Liu X J, Zhao W, Zhang Y and Zhu Z H 2016 Detecting relic gravitational waves by pulsar timing arrays: effects of cosmic phase transitions and relativistic free-streaming gases *Phys. Rev.* D **93** 024031

[8] Saikawa K i and Shirai S 2018 Primordial gravitational waves, precisely: the role of thermodynamics in the standard model *J. Cosmol. Astropart. Phys.* JCAP05(2018)035

[9] Deryagin D V, Grigoriev D Y, Rubakov V A and Sazhin M V 1987 Generation of gravitational waves by the anisotropic phases in the early universe *Mon. Not. R. Astron. Soc.* **229** 357

[10] Kahniashvili T, Brandenburg A, Gogoberidze G, Mandal S and Roper Pol A 2021 Circular polarization of gravitational waves from early-universe helical turbulence *Phys. Rev. Res.* **3** 013193

[11] Witten E 1984 Cosmic separation of phases *Phys. Rev.* D **30** 272

[12] Hogan C J 1986 Gravitational radiation from cosmological phase transitions *Mon. Not. R. Astron. Soc.* **218** 629

[13] Kamionkowski M, Kosowsky A and Turner M S 1994 Gravitational radiation from first-order phase transitions *Phys. Rev.* D **49** 2837

[14] Barausse E *et al* 2020 Prospects for fundamental physics with LISA *Gen. Rel. Grav.* **52** 81

[15] Dimopoulos S, Graham P W, Hogan J M, Kasevich M A and Rajendran S 2009 Gravitational wave detection with atom interferometry *Phys. Lett.* B **678** 37

[16] Caprini C, Durrer R and Siemens X 2010 Detection of gravitational waves from the QCD phase transition with pulsar timing arrays *Phys. Rev.* D **82** 063511

[17] Ellis J A, Jenet F A and McLaughlin M A 2012 Practical methods for continuous gravitational wave detection using pulsar timing data *Astrophys. J.* **753** 96

[18] Capozziello S, Khodadi M and Lambiase G 2019 The quark chemical potential of QCD phase transition and the stochastic background of gravitational waves *Phys. Lett.* B **789** 626

[19] Arzoumanian Z *et al* 2020 The NANOGrav 12.5 yr data set: search for an isotropic stochastic gravitational-wave background *Astrophys. J. Lett.* **905** L34

[20] Ratzinger W and Schwaller P 2021 Whispers from the dark side: confronting light new physics with NANOGrav data *SciPost Phys.* **10** 047

[21] Neronov A, Pol A R, Caprini C and Semikoz D 2021 NANOGrav signal from magnetohydrodynamic turbulence at the QCD phase transition in the early Universe *Phys. Rev.* D **103** L041302

[22] Abe K T, Tada Y and Ueda I 2020 Induced gravitational waves as a cosmological probe of the sound speed during the QCD phase transition (arXiv:2010.06193 [astro-ph.CO])

[23] Kitajima N, Soda J and Urakawa Y 2021 Nano-Hz gravitational wave signature from axion dark matter *Phys. Rev. Lett.* **126** 121301

[24] Ramberg N and Visinelli L 2021 The QCD axion and gravitational waves in light of NANOGrav results *Phys. Rev.* D **103** 063031

[25] Li S L, Shao L, Wu P and Yuv H 2021 NANOGrav signal from first-order confinement/deconfinement phase transition in different QCD matters (arXiv:2101.08012 [astro-ph.CO])

[26] Gorghetto M, Hardy E and Nicolaescu H 2021 Observing invisible axions with gravitational waves (arXiv:2101.11007 [hep-ph])

[27] Brandenburg A, Clarke E, He Y and Kahniashvili T 2021 Can we observe the QCD phase transition-generated gravitational waves through pulsar timing arrays? (arXiv:2102.12428 [astro-ph.CO])

[28] He Y, Brandenburg A and Sinha A 2021 Spectrum of turbulence-sourced gravitational waves as a constraint on graviton mass (arXiv:2104.03192 [gr-qc])

[29] Garcia-Bellido J, Murayama H and White G 2021 Exploring the early universe with Gaia and THEIA (arXiv:2104.04778 [hep-ph])

[30] Sesana A 2013 Systematic investigation of the expected gravitational wave signal from supermassive black hole binaries in the pulsar timing band *Mon. Not. R. Astron. Soc.* **433** 1

[31] Middleton H, Sesana A, Chen S, Vecchio A, Del Pozzo W and Rosado P A 2021 Massive black hole binary systems and the NANOGrav 12.5 year results *Mon. Not. R. Astron. Soc. Lett.* **502** 1

[32] Caprini C and Figueroa D G 2018 Cosmological backgrounds of gravitational waves *Class. Quantum Grav.* **35** 163001

[33] Durrer R, Ferreira P G and Kahniashvili T 2000 Tensor microwave anisotropies from a stochastic magnetic field *Phys. Rev.* D **61** 043001

[34] Kosowsky A, Mack A and Kahniashvili T 2002 Gravitational radiation from cosmological turbulence *Phys. Rev.* D **66** 024030

[35] Melatos A and Peralta C 2010 Gravitational radiation from hydrodynamic turbulence in a differentially rotating neutron star *Astrophys. J.* **709** 77

[36] Lasky P D 2015 Gravitational waves from neutron stars: a review *Publ. Astron. Soc. Aust.* **32** e034

[37] Neronov A and Vovk I 2010 Evidence for strong extragalactic magnetic fields from Fermi observations of TeV blazars *Science* **328** 73

[38] Archambault S *et al* (VERITAS Collaboration) 2017 search for magnetically broadened cascade emission from blazars with VERITAS *Astrophys. J.* **835** 288

[39] Ackermann M *et al* (Fermi-LAT Collaboration) 2018 The search for spatial extension in high-latitude sources detected by the Fermi large area telescope *Astrophys. J. Suppl.* **237** 32

[40] Arlen T C, Vassilev V V, Weisgarber T, Wakely S P and Shafi S Y 2014 Intergalactic magnetic fields and gamma-ray observations of extreme TeV blazars *Astrophys. J.* **796** 18

[41] Broderick A E, Tiede P, Chang P, Lamberts A, Pfrommer C, Puchwein E, Shalaby M and Werhahn M 2018 Missing gamma-ray halos and the need for new physics in the gamma-ray sky *Astrophys. J.* **868** 87

[42] Alves Batista R, Saveliev A and de Gouveia Dal Pino E M 2019 The impact of plasma instabilities on the spectra of TeV blazars *Mon. Not. R. Astron. Soc.* **489** 3836

[43] Ahonen J and Enqvist K 1996 Electrical conductivity in the early universe *Phys. Lett.* B **382** 40

[44] Brandenburg A, Enqvist K and Olesen P 1996 Large-scale magnetic fields from hydromagnetic turbulence in the very early universe *Phys. Rev.* D **54** 1291

[45] Brandenburg A, Kahniashvili T, Mandal S, Roper Pol A, Tevzadze A G and Vachaspati T 2019 Dynamo effect in decaying helical turbulence *Phys. Rev. Fluids* **4** 024608

[46] Kahniashvili T, Gogoberidze G and Ratra B 2005 Polarized cosmological gravitational waves from primordial helical turbulence *Phys. Rev. Lett.* **95** 151301

[47] Kuzmin V A, Rubakov V A and Shaposhnikov M E 1985 On anomalous electroweak baryon-number non-conservation in the early universe *Phys. Lett.* B **155** 36

[48] Shaposhnikov M E 1986 Possible appearance of the baryon asymmetry of the universe in an electroweak theory *JETP Lett.* **44** 465

[49] Cohen A G, Kaplan D B and Nelson A E 1990 Weak scale baryogenesis *Phys. Lett.* B **245** 561

[50] Cohen A G, Kaplan D B and Nelson A E 1991 Baryogenesis at the weal phase transition *Nucl. Phys.* B **349** 727

[51] Morrissey D E and Ramsey-Musolf M J 2012 Electroweak baryogenesis *New J. Phys.* **14** 125003

[52] Hindmarsh M, Huber S J, Rummukainen K and Weir D J 2014 Gravitational waves from the sound of a first order phase transition *Phys. Rev. Lett.* **112** 041301

[53] Hindmarsh M and Hijazi M 2019 Gravitational waves from first order cosmological phase transitions in the sound shell model *J. Cosmol. Astropart. Phys.* JCAP12(2019)062

[54] Christensson M, Hindmarsh M and Brandenburg A 2001 Inverse cascade in decaying 3D magnetohydrodynamic turbulence *Phys. Rev.* E **64** 056405

[55] Kahniashvili T, Brandenburg A, Tevzadze A G and Ratra B 2010 Numerical simulations of the decay of primordial magnetic turbulence *Phys. Rev.* D **81** 123002

[56] Vachaspati T 2020 Progress on cosmological magnetic fields (arXiv:2010.10525 [astro-ph.CO])

[57] Lifshitz E 1946 Republication of: on the gravitational stability of the expanding universe *J. Phys. (USSR)* **10** 116
Lifshitz E 2017 *Gen. Relativ. Gravit.* **49** 18

[58] Grishchuk L P 1975 Amplification of gravitational waves in an isotropic universe *Sov. Phys. JETP* **40** 409

Grishchuk L P 1974 *Zh. Eksp. Teor. Fiz.* **67** 825

[59] Mukhanov V, Feldman H A and Brandenberger R H 1992 Theory of cosmological perturbations *Phys. Rep.* **215** 203

[60] Durrer R and Kunz M 1998 Cosmic microwave background anisotropies from scaling seeds: generic properties of the correlation functions *Phys. Rev.* D **57** R3199

[61] Grasso D and Rubinstein H R 1996 Revisiting nucleosynthesis constraints on primordial magnetic fields *Phys. Lett.* B **379** 73

[62] Zrake J 2014 Inverse cascade of nonhelical magnetic turbulence in a relativistic fluid *Astrophys. J.* **794** L26

[63] Brandenburg A, Kahniashvili T and Tevzadze A G 2015 Nonhelical inverse transfer of a decaying turbulent magnetic field *Phys. Rev. Lett.* **114** 075001

[64] Brandenburg A and Nordlund Å 2011 Astrophysical turbulence modeling *Rep. Prog. Phys.* **74** 046901

[65] Brandenburg A and Kahniashvili T 2017 Classes of hydrodynamic and magnetohydrodynamic turbulent decay *Phys. Rev. Lett.* **118** 055102

[66] Roper Pol A, Mandal S, Brandenburg A, Kahniashvili T and Kosowsky A 2020 Numerical simulations of gravitational waves from early-universe turbulence *Phys. Rev.* D **102** 083512

[67] Miniati F, Gregori G, Reville B and Sarkar S 2018 Axion-driven cosmic magnetogenesis during the QCD crossover *Phys. Rev. Lett.* **121** 021301

[68] Kahniashvili T, Brandenburg A, Campanelli L, Ratra B and Tevzadze A G 2012 Evolution of inflation-generated magnetic field through phase transitions *Phys. Rev.* D **86** 103005

[69] Mee A J and Brandenburg A 2006 Turbulence from localized random expansion waves *Mon. Not. R. Astron. Soc.* **370** 415

[70] Kadomtsev B B and Petviashili V I 1973 Acoustic turbulence *Sov. Phys. Dokl.* **18** 115

[71] Gogoberidze G, Kahniashvili T and Kosowsky A 2007 The spectrum of gravitational radiation from primordial turbulence *Phys. Rev.* D **76** 083002

[72] Kahniashvili T, Gogoberidze G and Ratra B 2008 Gravitational radiation from primordial helical MHD turbulence *Phys. Rev. Lett.* **100** 231301

[73] Brandenburg A and Boldyrev S 2020 The turbulent stress spectrum in the inertial and subinertial ranges *Astrophys. J.* **892** 80

[74] Roper Pol A, Brandenburg A, Kahniashvili T, Kosowsky A and Mandal S 2020 The timestep constraint in solving the gravitational wave equations sourced by hydromagnetic turbulence *Geophys. Astrophys. Fluid Dyn.* **114** 130

[75] Caprini C, Durrer R and Kahniashvili T 2004 The Cosmic microwave background and helical magnetic fields: the tensor mode *Phys. Rev.* D **69** 063006

[76] Monin A S and Yaglom A M 1971 *Statistical Fluid Mechanics Mechanics of Turbulence* vol 2 (Cambridge, MA: MIT Press)

[77] Falkovich G 1994 Bottleneck phenomenon in developed turbulence *Phys. Fluids* **6** 1411

[78] Stein R F 1967 Generation of acoustic and gravity waves by turbulence in an isothermal stratified atmosphere *Sol. Phys.* **2** 385

[79] Dobler W, Haugen N E L, Yousef T A and Brandenburg A 2003 The bottleneck effect in three-dimensional turbulence simulations *Phys. Rev.* E **68** 026304

[80] Brandenburg A *et al* (Pencil Code Collaboration) 2021 The Pencil code, a modular MPI code for partial differential equations and particles: multipurpose and multiuser-maintained *J. Open Source Softw.* **6** 2807

[81] Kahniashvili T, Brandenburg A, Gogoberidze G, Mandal S and Roper Pol A 2020 Datasets for circular polarization of gravitational waves from early-universe helical turbulence see also http://www.nordita.org/~brandenb/projects/CircPol/ for easier access

[82] Brandenburg A, Clarke E, He Y and Kahniashvili T 2021 Datasets for can we observe the QCD phase transition-generated gravitational waves through pulsar timing arrays? see also http://www.nordita.org/~brandenb/projects/GWfromQCD/ for easier access